Organic Open-cell Porous Structure Modeling

Lihao Tian
Shandong University
tianlihao0420@gmail.com

Lin Lu*
Shandong University
llu@sdu.edu.cn

Weikai Chen
Tencent US
chenwk891@gmail.com

Yang Xia
Dalian University of Technology
yangxia@dlut.edu.cn

Charlie C. L. Wang
The University of Manchester
changling.wang@manchester.ac.uk

Wenping Wang
The University of Hong Kong
Wenping@cs.hku.hk

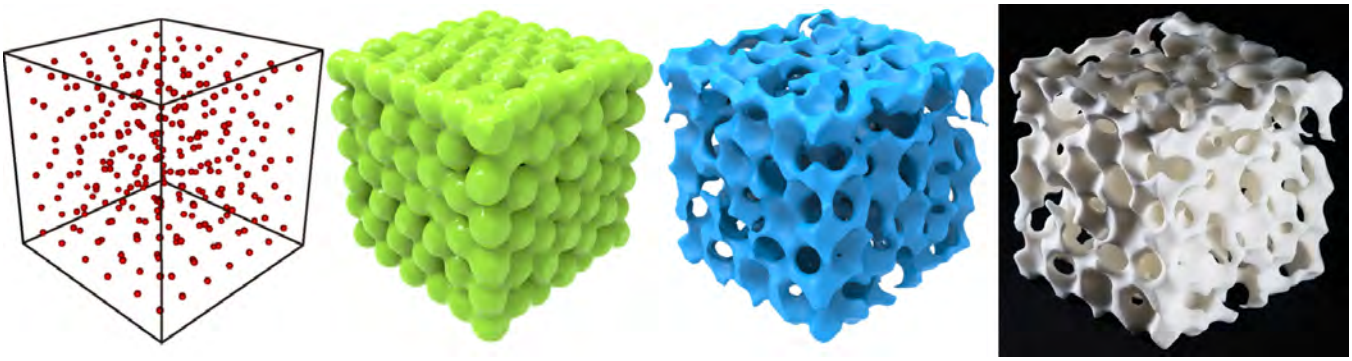

(a) (b) (c) (d)

Figure 1: Through the system of this article, from a distribution of particles (a), we optimize under the condition of ensuring its connectivity, and obtain the corresponding pore structure(b) and solid part(c) of the model. (d) shows the 3D printed result of the organic porous structure.

ABSTRACT

Open-cell porous structures are ubiquitous in nature and have been widely employed in practical applications. Additive manufacturing has enabled the fabrication of shapes with intricate interior structures; however, a computational method for representing and modeling general porous structures in organic shapes is missing in the literature. In this paper, we present a novel method for modeling organic and open-cell porous structures with porosities and pore anisotropies specified by users or stipulated by applications. We represent each pore as a transformed Gaussian kernel whose anisotropy is defined by a tensor field. The porous structure is modeled as a level surface of combined Gaussian kernels. We utilize an anisotropic particle system to distribute the Gaussian kernels concerning the input tensor field. The porous structure is then generated from the particle system by following the anisotropy specified by the input. We employ Morse-Smale complexes to identify the topological structure of the kernels and enforce pore connectivity. The resulting porous structure can be easily controlled using a set of parameters. We demonstrate our method on a set of 3D models whose tensor field is either predesigned or obtained from the mechanical analysis.

CCS CONCEPTS

• **Computing methodologies** → **Shape modeling**; *Modeling and simulation.*

KEYWORDS

porous structure, tensor field, Gaussian kernel, Morse-Smale complex.

ACM Reference Format:
Lihao Tian, Lin Lu, Weikai Chen, Yang Xia, Charlie C. L. Wang, and Wenping Wang. 2020. Organic Open-cell Porous Structure Modeling. In *Symposium on Computational Fabrication (SCF '20), November 5–6, 2020, Virtual Event, USA.* ACM, New York, NY, USA, 12 pages. https://doi.org/10.1145/3424630.3425414

1 INTRODUCTION

Porosity is an integral property of natural structures. Stones and soils contain interconnected pores and channels that permit liquid and gas penetration. Porous media exhibit desirable physical properties, such as being lightweight or having high impact absorption; therefore, the properties and preparation methods of such media have been comprehensively studied [Gibson and Ashby 1999]. Porous materials are used in medical applications (bone substitutes and dentures), chemical engineering (catalyst carriers

*Corresponding author.

SCF '20, November 5–6, 2020, Virtual Event, USA

ACM ISBN 978-1-4503-8170-3/20/11…$15.00
https://doi.org/10.1145/3424630.3425414

and membranes for water treatment), civil engineering (concrete, fibrous assemblies, and structural materials), material engineering (metal foam, insulating materials, sound-absorbing coatings, and biomaterials), and tissue engineering.

Many attempts have been made over the years to reconstruct the geometric structures of porous media for analyzing effective properties and estimating material performance, through imaging or scanning procedures, or mathematical methods by simulating the fabrication process [Pant 2016]. The progress in 3D printing enables fabricating the complex geometries and further broadens the applications of porous structures at different scales. Thus, increasing efforts have been devoted to modeling and utilizing porous structures in various applications, including scaffold design for tissue engineering [Hollister 2005; Wu et al. 2011; Yoo 2011], and interior structures for mechanical optimization [Lu et al. 2014; Wu et al. 2017; Yan et al. 2019], etc.

Natural porous media like bones, reefs, and plants mostly possess two characteristics, curvilinear structures, and interconnected pores. Such features benefit both macroscopic physical properties and additive manufacturing. Organic pore architecture help avoid stress accumulation. Interconnected pores and solids make the models feasible to powder-based 3D printing techniques. However, existing porous modeling methods can hardly produce organic open-cell porous structures with capabilities of controlling the anisotropy, porosity, pore shape, etc.

In this paper, we attempt to propose a modeling framework for generating organic open-cell porous structures with controllable porous properties. Specifically, we represent each pore by a parameterized anisotropic Gaussian kernel, which possesses controllable organic shape and conforms to the given anisotropy. Then, the full connectivity of pores and solids is enforced with the guidance of the Morse-Smale complex (MSC), respectively. Given the pore shape, target porosity, and specified anisotropy, the porous structures could be produced to incarnate users' design using our modeling method. We further develop an optimization framework to drive the porous structures to the optimized internal surface area, and strength, etc.

Our contributions are as follows.

- We present a modeling framework that automatically generates organic open-cell porous structures, conforming to given tensor fields.
- Our algorithm guarantees the connectivity of both solids and pores via an MSC-based enforcement method and supports controllable porosity, density, and pore shapes.
- Our optimization framework can be adapted to different objectives, like the internal surface, mechanical properties, etc.

2 RELATED WORK

Porous structure reconstruction. Most 3D porous structure modeling techniques apply a reconstruction methodology to mimic the full or partial scale of existing porous structures. In general, these techniques apply statistical or stochastic models for reconstructing 3D porous media from 2D thin section images or 3D voxel data.

The sampled digitized serial sections are obtained by scanning electron microscopy (SEM) [Kwiecien et al. 1990; Whitehouse and Dyson 1974], high-resolution X-ray tomography (HRCT) [Dunsmuir et al. 1991], or micro-computed tomography (μCT) [Zhu et al. 2014]. 3D porous structures are obtained by either geometrical reconstructions [Pouech et al. 2010; Sun et al. 2005; Zhu et al. 2014], or texture synthesis [Holdstein et al. 2009; Liu and Shapiro 2015; Zhang et al. 2017]. Researchers in material science introduced physical process-based mimicking techniques, including infrared (IR) gas porosimetry, mercury intrusion porosimetry [Cernuschi et al. 2013], etc. A detailed description of existing reconstruction modeling methods for porous structure can be found in [Pant 2016]. Reconstruction methods rely on data acquisition and high computational cost, and can hardly realize the porous model's full-scale details.

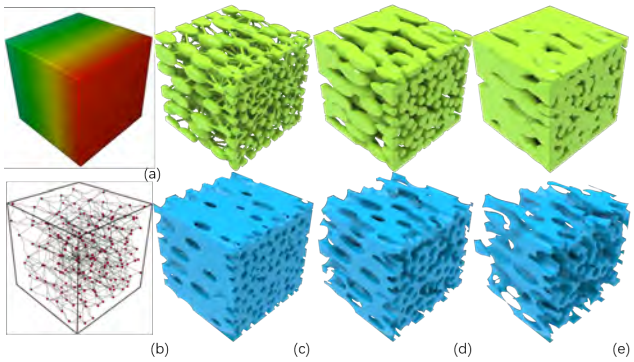

Figure 2: Given a 3D cuboid shape and a user-designed tensor field (a), we generate the corresponding interior-point distribution and compute the MSC structure (b). By using combined anisotropic Gaussian kernels, we obtain connected pores and solids (c-e), with varying porosity values of 20%, 50% and 80%, respectively. (The upper row displays the pores in the shape, in green; the lower row displays the corresponding left porous volume, in blue.)

Porous structure design. Stochastic methods stand in the classical group for modeling the porous structures with varying density and porosity properties close to the existing porous media. The basic idea is using a two-point probability function to represent a voxel to be grain or pore and then applying stochastic functions to generate the synthetic data. Stochastic functions include simulated annealing [Manwart et al. 2000], a pressure correction algorithm [Hilfer and Manwart 2001], Monte Carlo methods [Manwart and Hilfer 1999], CSG operations [Schroeder et al. 2005]. The local porosity distribution is controlled by a probability density function, which can generate organic pore shapes. [Mosser et al. 2017] attempted to train generative adversarial neural networks on segmented volumetric images for three-dimensional stochastic image reconstruction of porous media.

Spatial tessellations are also often used in porous modeling. Existing approaches employ Voronoi diagrams to tessellate the given shape in a stochastic and space-pleasing manner, and then model the pores via inscribed implicit curves or parametric B-splines [Kou and Tan 2012; Wyvill et al. 2012; Yaman et al. 2016]. [Lu et al. 2014] took centroidal Voronoi tessellations, represented

each Voronoi cell as a harmonic field, and carved with an optimized hollowness parameter in terms of the global strength-to-weight ratio. They only considered the von Mises value without the stress tensor's directions and produced an isotropic closed porous structure. To involve anisotropy in Voronoi-based porous structures, [Ying et al. 2018] proposed the anisotropic closed-cell porous modeling method, but only in 2.5D. [Martínez et al. 2016] proposed to generate aperiodic, stochastic open-cell Voronoi foams with prescribed isotropic elasticity, through a procedure akin to solid procedural textures. They extended isotropic structures into orthotropic foams [Martínez et al. 2017] and achieved k-nearest structures with good orthotropic elasticity. However, the basic structural element is the beam but not the organic anymore. In [Martínez et al. 2018], they further present the closed-cell, self-supported stochastic foams friendly to fused filament fabrication (FFF) based 3D printers. Recently, [Martínez et al. 2019] introduced the star-shaped metrics in Voronoi diagrams, such that more structures could be involved, and the range of mechanical properties is widened.

Both stochastic methods and spatial tessellations have advantages in representing organic pore shapes. Unfortunately, these methods share the same problem that porous connectivity is hard to achieve.

Topology optimizations have emerged as an option for porous modeling over recent years. However, the grain element is usually truss or lattice structures [Arora et al. 2019; Wang et al. 2013; Wu et al. 2016b]. [Wu et al. 2017] proposed a density-based approach to design bone-like porous structures via topology optimization under local material volume constraints. The authors further present a method to design lattice structures that conform with both the principal stress directions and the shape boundary [Wu et al. 2019]. Except for the inorganic pore shapes, the pore connectivity cannot be theoretically guaranteed for these methods.

Microstructure design and tiling can also produce porous structures [Chen et al. 2018; Tozoni et al. 2020]. Families of periodic microstructure tiles with varying properties are predesigned through an inverse homogenization problem [Sigmund 1994]. Then, they can be easily synthesized to fulfill target functionalities [Panetta et al. 2015; Schumacher et al. 2015]. Nevertheless, such microstructure does not satisfy organic properties.

To our knowledge, existing porous modeling methods can barely generate the porous structures that fulfill all the objectives we tackled, i.e., organic pore shape, connectivity for both pores and solids, and conforming to the given tensor field.

Tensor field sampling. The modeling process of our study is primarily driven by a user-defined tensor field or a stress field obtained from the mechanical analysis. Therefore, the tensor field design is critical to the outcome of a porous structure. Tensor fields have been adequately researched in terms of mathematical and numerical analyses. Moreover, tensor field visualization has been well developed for postprocessing applications for computational mechanics by the scientific visualization community [Neeman et al. 2005]. [Zhang et al. 2007] present an interactive design system that allows users to create a wide variety of symmetric tensor fields over 3D surfaces either from scratch or by modifying a meaningful input tensor field such as the curvature tensor. [Palacios et al. 2017] provided a 3D tensor field design system, which can edit the topology of the tensor fields. On the basis of these studies, a meaningful tensor field is regarded as a reasonable input for porous modeling.

Gaussian kernels have strong capabilities to fit in a given shape and are widely used in many applications. In the realm of signal processing, Gaussian kernels are used as a basis function to approximate an arbitrary signal and reconstruct sparse signals through matching pursuit methods. In numerical simulations, Gaussian kernels act as the Green's function for the diffusion equation.

Under Gaussian kernels, a particle denotes the center of a peak, and accordingly determines pore position. With the technology of anisotropic centroidal Voronoi tessellations [Du and Wang 2005], anisotropic meshing [Zhong et al. 2013] or anisotropic blue noise sampling [Li et al. 2010], the particle could be sampled in a pattern driven by a user-defined anisotropy field for a given volume.

Morse-Smale Complex analysis. The Morse-Smale Complex (MSC) is a topological structure that captures the gradient behavior of a scalar function on a manifold. The MSC decomposes the domain into monotonic regions associated with the critical points of the function, indicating the smallest topological features. As a natural and mathematically sound tool, the Morse-Smale complex is widely used for topology-based shape analysis and understanding, and thus supporting various applications, such as surface smoothing, segmentation, compression and visualization [Čomić et al. 2013; De Floriani et al. 2015; Edelsbrunner et al. 2003; Gyulassy and Natarajan 2005; Ling et al. 2014] etc. Moreover, the efficient computation of a 3D MSC has gained considerable attention [Gyulassy et al. 2007; Shivashankar and Natarajan 2012].

3 OVERVIEW

Given a 3D shape $\Omega \subset \mathbb{R}^3$ defined by a boundary surface mesh, in addition to a second-order tensor field, our method generates porous structures that are consistent with the tensor field in terms of both the magnitude and directional features of the tensor field. Our modeling framework intends to drive the porous structures to the target porosity, cell size, maximal surface area, with the constraints that both pores and solids are fully connected.

We employ the transformed Gaussian kernel conforming to the given tensor in terms of both magnitudes and directions. We regard the initial tensor field as an underlying field, where each sample point has a 3×3 symmetric tensor matrix; see Fig. 2a. We consider this matrix as an anisotropic local metric, and generate a varying point distribution by utilizing the generalized Poisson disk property through dart-throwing and relaxation algorithms; see Fig. 2b. With the point distribution, we fit each point with an anisotropic Gaussian kernel function defined by the local tensor metric and the variance parameter. Subsequently, we construct the level surface with a level set value to represent the porous surfaces.

The overall porous structure is determined by the kernel distributions P and their scales K. The two sets of variables are optimized according to the objectives, like porosity, cell size, surface area, etc. (Fig. 2c-g).

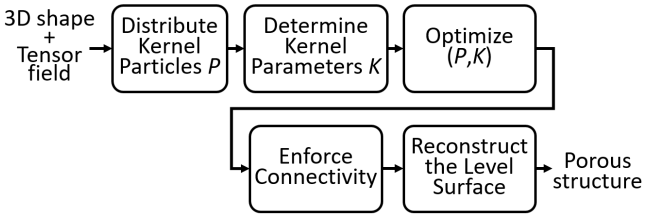

Figure 3: The flow chart of the porous modeling framework.

To ensure that the pores and solids are both fully interconnected, we compute the MSCs within Ω to identify the topological structures and employ it as the guidance for connectivity enforcement. The Gaussian function defined over the given space is directly employed as the volumetric Morse function. Thus, critical points (maxima, minima, 1-saddle, and 2-saddle) can be extracted accordingly, in which the maxima coincide with the kernel centers. Once the ascending and descending manifold cells are computed (Fig. 2b), we have the full guidance for constructing connections between the isolated pores or solid and their topological neighbors. A smooth, adaptive blending tunnel between the kernels based on a Bernstein basis function is added to enforce the connectivity.

The discretized form is used for the efficiency of both MSC computation and implicit surface reconstruction. After the optimization and connectivity enforcement, the porous structure is reconstructed via marching cubes. Fig. 3 shows the flow of the porous modeling framework.

4 ANISOTROPIC GAUSSIAN KERNEL

4.1 Tensor Field Defined Anisotropy

Anisotropy implies different properties in different directions. In this paper, we use a tensor-based metric for representing anisotropy. Local anisotropy can be defined by three orthogonal principal directions and an aspect ratio in each direction. The local metric of each point in the domain Ω is defined by a symmetric tensor matrix T. The matrix T can be decomposed into

$$T = R\Lambda R^{\mathrm{T}}, \tag{1}$$

where Λ is a diagonal matrix that contains ordered eigenvalues, and the columns of the orthogonal matrix R are the respective eigenvectors. The matrix R defines the rotation of the local frame while Λ represents the scaling of three principal axes. Fig. 4 illustrates the transformation defined by T.

The distance between two points p_i and p_j under anisotropic metric T is expressed by

$$\left|p_i, p_j\right|_T = \sqrt{\left(p_i - p_j\right)^{\mathrm{T}} T \left(p_i - p_j\right)}. \tag{2}$$

In Fig. 2, we use a simple user-defined tensor field, where each point shares the same anisotropic ratio, with the scaling factor proportional to its axial length from the origin at the corner. We compute the Frobenius norm for each tensor matrix and color code it in Fig. 2a.

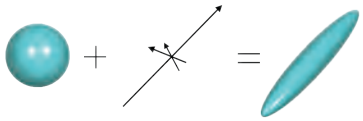

Figure 4: Iso-surface of the same distance from a point would change from sphere (left) to an ellipsoid (right) if the anisotropic metric is applied.

4.2 3D Anisotropic Gaussian Kernel

The basic 3D isotropic Gaussian kernel centered at point p_i is defined as

$$G_i(p) = \frac{1}{\left(\sqrt{2\pi}\cdot k_i\right)^3} e^{-\frac{\|p-p_i\|^2}{2{k_i}^2}}, \tag{3}$$

where $k_i > 0$ determines the width of the Gaussian kernel at p_i and $\|\cdot\|$ denotes the Euclidean norm.

By considering the general case of an oriented anisotropic Gaussian function, we apply the anisotropic metric defined in Section 4.1 and obtain the 3D anisotropic Gaussian kernel at point p_i with the tensor matrix T_i as follows:

$$G_i^A(p) = \frac{1}{(\sqrt{2\pi\xi}k_i)^3} e^{-\frac{(p-p_i)^{\mathrm{T}} T_i (p-p_i)}{2k_i^2}}, \tag{4}$$

where $\xi = \frac{1}{\lambda_1\lambda_2\lambda_3}$, and $\lambda_1, \lambda_2, \lambda_3$ represent the ordered eigenvalues of T_i. The variable k_i is for flexibly controlling the shape of the Gaussian kernel.

4.3 Combined Gaussian Kernels

Given n Gaussian kernels centered on $\{p_i\}_{i=1}^n$, we define the combined function $F : \mathbb{R}^3 \to \mathbb{R}$ for every point $p \in \Omega$ as

$$F(p) = \sum_i G_i^A(p). \tag{5}$$

This combined function is regarded as the level set function. Once given a value $C \in \mathbb{R}^+$, a level surface can be extracted via $F(p) = C$.

Therefore, we represent our porous structure as a level surface determined by Equation 6, including three set of parameters, distribution of the particles $P = \{p_i\}_{i=1}^n$, scale of the kernels $K = \{k_i\}_{i=1}^n$, and the level set value C,

$$\sum_i G_i^A(p) = C. \tag{6}$$

Fig. 5 illustrates the idea in 2D in terms of the parameter C. There are three 2D Gaussian kernels with different variances generated from neighboring sites on a plane. Different level set values drives the level curve with different shapes. For one kernel, the level curve is an ellipse considering the anisotropic metric.

5 POROUS STRUCTURES MODELING

5.1 Kernel Distribution

To distribute the kernels conforming to the underlying tensor field, we optimize the distributions via a blue noise sampling

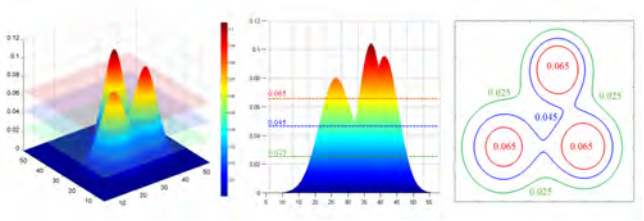

(a) (b) (c)

Figure 5: Combined 2D Gaussian kernel and its level set curve. (a) combined 2D Gaussian kernels cut by three level planes; (b) side view of (a); (c) three extracted level curves from (a).

method. First, we generate the initial particle distribution through anisotropic dart throwing. The particles are generated sequentially one by one. To determine the next particle's location, a trial sample is randomly generated from the input domain. If the new sample is at least a predefined distance from all existing samples, the particle is added to the domain. Note that the distance here is under anisotropic metric, which would lead to the anisotropic distribution of particles.

Then, we apply relaxations for the particles P via conventional 3D centroidal Voronoi tessellations (CVT) computation [Liu et al. 2009]. The objective function is

$$\mathcal{F}(P) = \sum_{i=1}^{n} \int_{p \in \Omega_i} (p - p_i)^{\mathrm{T}} T (p - p_i) \, \mathrm{d}p, \tag{7}$$

where Ω_i is the Voronoi region for p_i clipped by the given shape boundary $\partial\Omega$. There are two subroutines of the relaxation: Lloyd method and LBFGS optimization. In Lloyd subroutine, the particle is moved to the centroid of its affiliated cell in each iteration. After each iteration, particles tend to be distributed in a more regular form while maintaining the random property of blue noise sampling. However, the LBFGS method has a much faster convergence speed compared to the Lloyd method. The target problem of Limited-memory variant of Broyden-Fltcher-Goldfarb-Shanno (LBFGS) method as described in [Nocedal and Wright 2006] is to minimize the differentiable scalar function 7 and get each p_i. We use limited steps of LBFGS iterations to refine particle distributions in those scenarios which regular patterns are more appreciated.

Generally, when modeling complex tissue structures, the Lloyd method can better depict the overall randomness while following underlying patterns. LBFGS routine would be applied if the input patterns need to be strictly followed. Fig. 2b shows the anisotropic particle distribution generated based on our framework.

5.2 Kernel Variance

As discussed, besides $\{p_i\}_{i=1}^n$, the level surface is determined by $\{k_i\}_{i=1}^n$ and C. Essentially, these two sets of variables are correlated. Specifically, while keeping one of $\{k_i\}_{i=1}^n$ and C unchanged, adjusting the other can change the pore size. Also for this reason, the initial value of C can be chosen at will. To obtain more controlling capabilities, we set $\{k_i\}_{i=1}^n$ as the variables and C as the parameter ($C = 1$ in our experiments). After the value of C is fixed, $\{p_i\}_{i=1}^n$

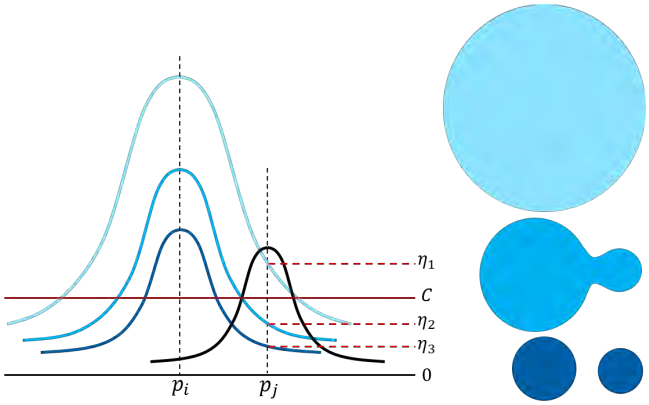

Figure 6: Illustrations on the effectiveness of the parameter η. Larger η indicates the larger influence of the kernel (the light blue contour on the right.) ($\eta_1 > \eta_2 > \eta_3$) In the case of η_3, p_i-kernel swallows p_j-kernel.

and $\{k_i\}_{i=1}^n$ are independent variables, which together control the porous structure.

To facilitate the optimization on the kernel variance, it is worth to put efforts in initializing the variance value for k_i. The kernel's scale needs to coincide with its local tensor and neighborhood. For example, if several kernels are close to each other and one kernel has a large scale, then the level surface would be dominated by the large scale kernel and lose the porous feature. Therefore, in order to ensure that the porous structure is organic and each pore is guaranteed to be independently identified, we introduce a *dominance parameter* η as the upper bound to locally determine each k_i value. Intuitively, η indicates the dominant range for each kernel and thus reflects the local porosity around the kernel. Practically, for a kernel at p_i, we search the closest neighboring kernel point p_j in terms of the anisotropic distance metric defined by T_i as follows

$$p_j = \arg\min_{j \neq i} ((p_j - p_i)^{\mathrm{T}} T_i (p_j - p_i)). \tag{8}$$

Then we solve k_i for the kernel p_i by

$$G_i^A(p_j) = \frac{1}{(\sqrt{2\pi\xi}k_i)^3} e^{-\frac{(p_j - p_i)^{\mathrm{T}} T_i (p_j - p_i)}{2k_i^2}} = \eta C. \tag{9}$$

The dominance parameter η is represented by the standard deviations in the normal distribution. Empirically, we set $\eta = 2\sigma$, which means the probability that the values larger than 2 standard deviations away from the mean for the normal distribution, i.e. $\eta = 4.55\%$.

Fig. 6 illustrates the effectiveness of the η values. If η is too large, the neighboring pore might be "swallowed". If η is too small, it shrinks the design space.

Fig. 7 shows level surfaces of combined anisotropic 3D kernels under different values of variance K in a unit cube.

5.3 MSC-based Connectivity Enforcement

To generate an open-cell porous structure, all pores and solid materials must be interconnected. I.e., for both pore and solid part,

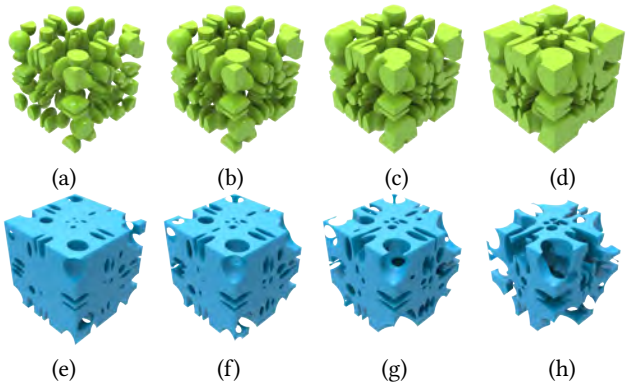

Figure 7: Kernels (n=250) are adaptively distributed in a unit cube under the tensor field, defined by the position vector for each sample point. From left to right, K increases and the porosity ρ = 43.6%, 54.3%, 67.1%, 74.0%, respectively.

they form one single component. Level surfaces derived in the preceding section have no guarantees on the full-connectivity. Thus, we need additional treatment to enforce connectivity.

Generally, there are two ways to control the pore connectivity, modulating the iso-surface value, or identifying neighboring pores and making connectivity. The iso-surface method cannot adapt to the complex local geometry due to the global influence of the iso-value. The local connectivity enforcement strategy relies on an efficient and effective way of exploring the local neighborhood. Heuristics methods, like the minimum spanning tree (MST), can hardly identify all local neighborhoods. The irregularly distributed anisotropic pores make the problem even hard.

To this end, we employ the Morse-Smale Complex (MSC) for identifying the local neighborhood, which has proven to be a simple and effective solution, without the pain of parameter tweaking. Then we enforce the full connectivity with the guidance from MSC, constructing connections between pores rationally and automatically.

5.3.1 MSC computation. We consider Equation 5 as the Morse function defined over the bounded volumetric space, and follow the method in [Gyulassy et al. 2007] for MSC computation. An MSC in a 3-manifold contains four types of critical points of the function, called minimum, 1-saddle, 2-saddle, and maximum. The complex decomposes the space into monotonic regions, which can be regarded as an overlay of ascending and descending manifolds.

Maxima in the MSC naturally coincide with the kernel positions. We identify the 2-saddles and trace the integral lines between two maxima crossing a 2-saddle point. If there is an integral path between two maxima, it indicates that the two corresponding kernels are topological neighbors. Similarly, the solid part contains minima. Two minima are topological neighbors if they are connected by an integral path crossing a 1-saddle point. Therefore, the MSC result coincides with the existing connections of kernels. Fig. 8(a) and (b) display the MSC results in ascending and descending manifolds respectively, for 40 kernels in the uniform and isotropic tensor field, where minimum, 1-saddle, 2-saddle and maximum are represented by blue, yellow, green and red dots, respectively.

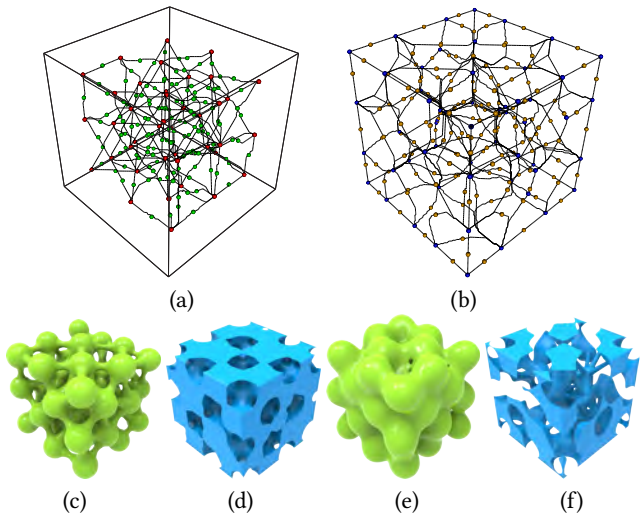

Figure 8: MSC structures for 40 kernels in a uniform isotropic tensor field, consisting of maxima (red) and 2-saddles (green) in (a), minima (blue) and 1-saddles (yellow) in (b). Tunnel construction in pores (c) and its related solid (d). Tunnel construction in solid (f) and its related pores (e).

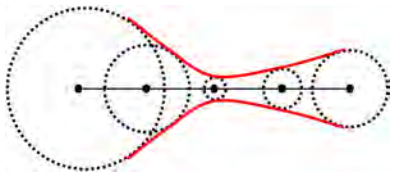

Figure 9: Illustration on constructing connections between two kernels.

5.3.2 Connection construction. With the global neighboring information from MSC, we cast the full connectivity enforcement problem into constructing extra connections between two neighbors. I.e., we create a "tunnel" between two pores if they are not connected and their corresponding kernels are neighbors in MSC.

To smoothly blend the two pores, we construct the tunnel in the form of fat curves [Mestetskii 2000]. A fat curve is a curve having a width; it is the trace left by a moving circle of a variable radius in 2D. We build a parametric function on the radius to control the tunnel shape, using the Bernstein basis polynomials of degree $n = 4$,

$$\mathbf{R}(t) = \sum_{i=0}^{n} B_{i,n}(t)\mathbf{r}_i, \quad 0 \le t \le 1,$$

where $B_{i,n}(t) = \binom{n}{i} t^i (1-t)^{n-i}, \quad i = 0, \ldots, n$, and $\mathbf{r}_i$ is the control point in term of radius of a sphere in 3D.

We reconstruct the exterior envelope of the family of spheres defined by $\mathbf{R}(t)$. As illustrated in Fig. 9, for two kernels, we sample five control points uniformly on the line segment connecting the kernel centers, and assign the radius on each control point. In practice, we set the radius for the two endpoints as the radius of the inscribed sphere of the corresponding pore. Then the radius on the middle, i.e., the minimal radius, is set according to the

fabrication and application constraints to ensure the printability and conductivity. For example, the minimal radius value is determined by the pore size, usually given by users.

For combining fat curves and the combined Gaussian function, we create a combined function in the voxel space to represent fat curves. The function values at the surface of the fat curves are C so that we can carve out the curves with width controlled via the Bernstein basis polynomials. After this step, the selection of the final combined function value is to choose the maximum value of Function 5 and the combined function for fat curves. In this way, it can be ensured that both pores and connection structures are successfully expressed at the same time.

We also rely on the guidance of MSC to guarantee the connectivity of the solid parts. For the inner isolated solid parts, we generate tunnels to its neighboring minima in different solid parts.

Once the additional fat curves are settled, we use the combined function in Equation 5 to represent them. I.e., the function values at the surface of the fat curves are set as C such that the tunnels can be reconstructed simultaneously with the porous structures. Fig. 8 shows the tunnel construction results for pores (c-d) and solids (e-f), respectively.

We note that the fat curve is generated in terms of Euclidean distance to minimize the modulations on the porous structure. Moreover, although rarely happens, it is theoretically possible that the fat arcs connecting pores interact with those connecting solids. In this case, we keep the solid arc as long as the pore arc is redundant to that pore.

6 APPLICATIONS AND RESULTS

The porous structure is defined as $\mathcal{S}(P, K)$, driven by two sets of variables (P, K), where $P = (p_i)_{i=1}^n$ indicates the distribution of the transformed Gaussian kernels, n is the number of kernels, p_i represents the position for each kernel; and $K = (k_i)_{i=1}^n$, $k_i \in R^+$ controls the width of the kernel. To demonstrate the capabilities of variables (P, K), we plot the relationships between the variables and porosity, surface area, respectively. For the sake of simplicity, we take a constant, isotropic tensor field within a unit cube as the input, and generate the porous structures varying in the number of kernels and the uniform width for all kernels. We compute the porosity and surface area for each porous structure and plot the modeling space, shown in Fig. 10. The porosity is of positive correlation with K and n, when fixing the other set of variables. The relationship between the surface area and n is positive with a fixed K. The porosity of the structures with the maximal surface area is around 50%. We note that the MSC arcs do not play into the optimization framework. Whenever the optimization is done, we check and enforce the connectivity. In order to explore the potential of our organic porous structure modeling framework in various fields, we tried a variety of applications and optimization problems with different objectives.

6.1 Porosity and Cell Size Control

In applications such as the implant design, there are constraints on the target porosity and cell size. This can be solved as a search problem from (P, K) in the modeling framework. The porosity in this section refers to the ratio of the volume of the model entity to the total volume. For printability considerations, users are more concerned about the minimum size of the pores in the model. So we define the cell size as the length of the shortest axis in an ellipsoidal pore.

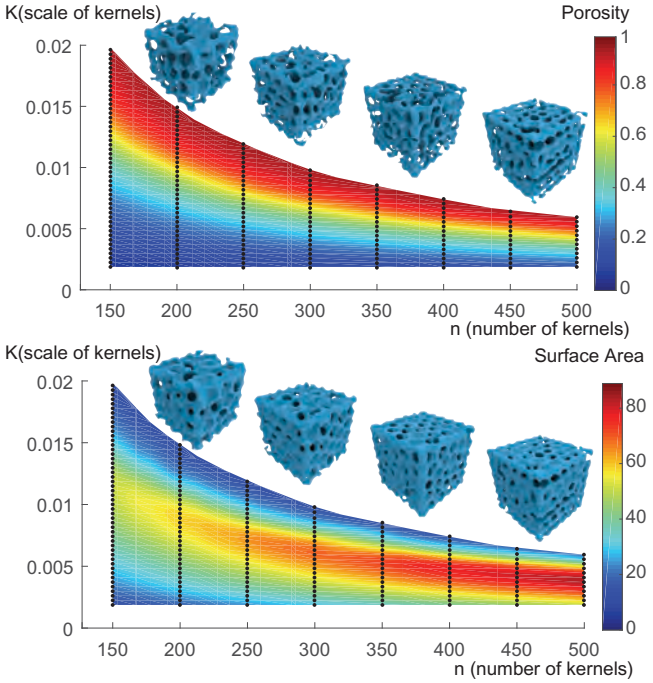

Figure 10: Illustrations on the modeling spaces of the porosity and surface area in the cube. Sample models are with 70% porosity and with the maximized surface area in two spaces respectively. Numbers of kernels are 200, 300, 400, 500 from left to right.

Suppose the cell size is γ. Then for the *i-th* kernel we first find the direction vector of the shortest axis of the local tensor denoted by x_i and then solve k_i such that $G_i^A(p_i + \frac{\gamma}{2}x_i) = C$. Since the kernel number n has a positive correlation with porosity when fixing K, we can obtain the target porosity by a linear search of n.

Fig. 11 lists some resulted porous structures with the target porosity and cell size in a designed tensor field.

6.2 User Design

We offer an easy-to-use interface for users to design porous structures in shapes with given tensor fields. We represent the porous structures by three parameters, density(n), porosity(ρ), and shape of pores. Once users provide the parameter values, the porous structure can be automatically generated.

The modeling space is described by three axes, density of pores, porosity, and shape of pores. Density is controlled by P, i.e., the number of kernels. Specific porosity is achieved by K, as explained in Section 6.1. The shape of pores is open to users for creative design as well.

For a given shape, the tensor field can be predesigned by interactive tools like [Palacios et al. 2017]. Then we use the directions of the tensor field and permit users to adjust the shape

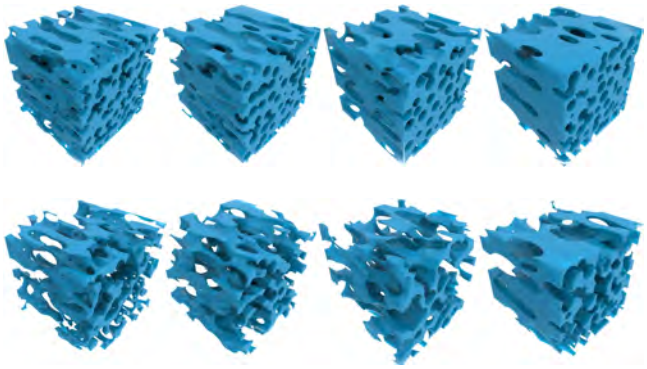

Figure 11: Different porous geometries with the same porosity under the tensor field as in Fig. 2. The porosity is 50% and 80% for the upper and lower row, respectively. The cell size increases from left to right.

of pores by selecting three eigenvalues of the tensor. Fig. 12 shows an example of varying parameters for the vase model, where we only show two dimensions of the design space, density, and shape of pores, as influences of porosity and density have been elaborated above. Fig. 13 shows some results. The pore shape of the bunny model is isotropic. The pore shape in the other two figures is the most anisotropic in the space of Fig. 12. The tensor fields for the double-torus and vase model are designed by [Palacios et al. 2017]. The tensor field guides the overall trend of anisotropic pore arrangement.

6.3 Surface Area Optimization

The surface area is a critical issue for porous media. The large area benefits several physical properties like heat dissipation, permeability, and tissue ingrowth. From the modeling space, the larger number of kernels there is, the larger surface area we will achieve. While, the kernel number is bounded by the fabrication capability like the printing feature size. We propose the optimization that maximizes the surface area of the current porous structure by tuning (P, K) without changing the number of kernels. The formulation is as follows,

$$\underset{P,K}{\operatorname{argmax}} A_{\mathcal{S}}(P, K), \tag{10}$$

where $A_{\mathcal{S}}(P, K)$ represents the area of the porous structure $\mathcal{S}$. We employ a gradient descent optimization to maximize the area, in which the approximated gradient of P and K is computed by numerical differentiation. Fig. 14 shows an example of the optimized porous structure on its surface area. The change of surface area and porosity along with iterations is plotted. We remark that the surface area optimization is an exception of the flow in Fig 3, as the surface reconstruction is needed for each iteration.

6.4 Strength Optimization

Given the 3D shape and its working conditions including external forces and boundary conditions, we follow the same goal as in the state-of-the-art structural optimization frameworks [Lu et al. 2014; Wang et al. 2013], to design the inner structures and maximize the

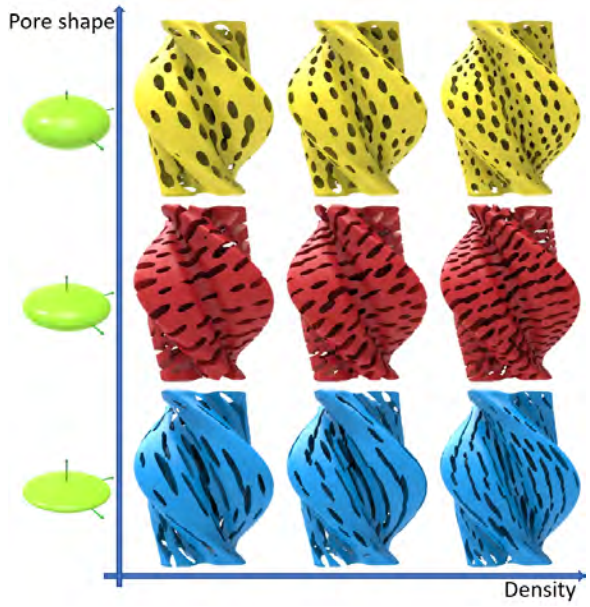

Figure 12: An example of the design of the porous structure in the vase model, whose tensor field is from [Palacios et al. 2017]. The horizontal axis shows the increasing of the density value from $n = 250$ to $n = 920$. The vertical axis lists three settings for the shapes of pores. The porosity is 50% for all.

strength-to-weight ratio. The objective function can be formulated into achieving the lightest interior that sustains given forces, via variables (P, K).

However, in order to ensure the organic properties of the porous structure, we control the pores to be fully expressed during optimization. Therefore, we use the η introduced in Section ref-sub:levelSurface to calculate the upper bound of K to initialize the optimization process.

We assume single uniform isotropic materials and Hooke's linear elastic model in the FEM computation, where we regard a voxel as the primary element. For each element, we have a Cauchy stress tensor from the FEM analysis.

Denote $V_{\mathcal{S}}(P, K)$ as the volume function of the structure $\mathcal{S}$ determined by (P, K). We formulate the search for the lightest interior with the target porosity ρ_0 into a constrained optimization,

$$\underset{P,K}{\operatorname{argmin}} V_{\mathcal{S}}(P, K)\ s.t.\ SM(\mathcal{S}, F) < \chi\ \&\&\ \rho < \rho_0,$$

where $SM(\mathcal{S}, F)$ is the stress map computed by applying the forces F on $\mathcal{S}$. χ is the yielding point of a specific material (by default $\chi = 2.5e^7 N/m^2$ for plastic).

Starting from a dense distribution of kernels, we employ a stochastic gradient descent (SGD) strategy, to iteratively relieve the stress. It includes two loops of iterations. For each voxel, we compute its dominating Gaussian kernel, under which it has the largest Gaussian function value. In the inner loop, we traverse the voxel elements. If it is weak, i.e., the von Mises stress value is beyond the yielding point, then its dominating kernel is marked. After the

Figure 13: Results produced using different tensor field specified by users. Left: pores; Right: porous structures. Bunny: $n = 1650, \rho = 65\%$**; Double-torus:** $n = 1000, \rho = 50\%$**; Vase:** $n = 1650, \rho = 48\%$**.**

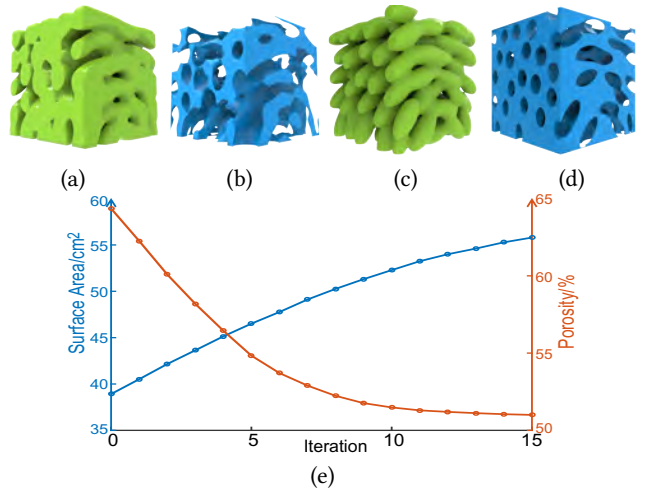

Figure 14: Optimizations on the surface area for the cube with edge 2cm. The surface area before optimization is $39cm^2$ **(b), and** $56cm^2$ **after optimization (d), gaining 44%. Plots of the surface area (blue curve) and porosity (orange curve) along with optimization iterations in (e).**

whole traversal, all marked Gaussian kernels decrease their width with one step size. The step size is set as the $0.25k_{\min}$, where $k_{\min}$ is the minimal value of all marked K. In the outer loop, we merge each very small kernel that is still associated with weak elements to its closest neighbor to gain materials and thus further relieve the stress. The stopping criteria are that no weak element is left, or the model becomes fully solid. Fig. 15 shows iterations of the porous structures in the femur model, with $\rho_0 = 70\%$.

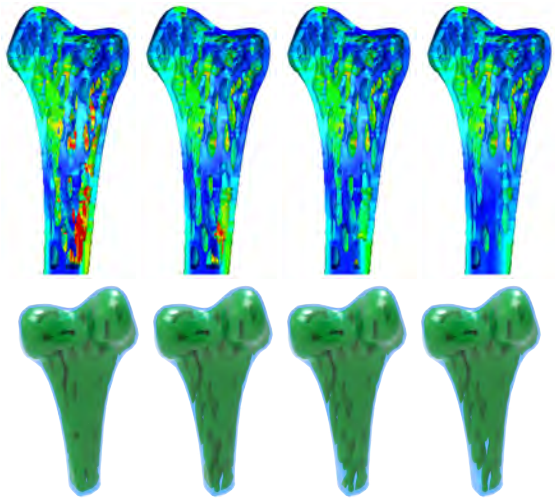

Figure 15: Optimization iterations for the femur model, targeting for both porous structure and mechanical properties.

6.5 Comparisons

We admit that our porous models do not outperform in terms of the strength-to-weight ratio comparing with the results from standard topology optimization methods. Fig. 16 shows the comparison among the result with a total volume constraint [Wu et al. 2016a], with local volume constraints [Wu et al. 2017] and ours. The three models are optimized with the same material properties and boundary conditions. Our result need a bit more materials to gain the same strength due to the Gaussian kernel representations. However, the classic topology optimization method has finer grain in deciding the occupancy of the materials, thus driving the porous into beam-like structures. We also compare a cubic sample from [Wu et al. 2017] and one from a human femur CT scans with ours in Fig. 17. It can be seen that our sample is visually similar to the natural bone sample, as our organic porous structures are more like cellular structures.

Since our porous structures have guaranteed full connectivity and optimized surface area, it would greatly benefit the design of biological implants. Requirements for the metallic implants include that, the mass is similar to that of the natural bone, and it allows existing biologic tissue to grow right into it.

Based on the consultation with medical doctors, for the vertebra, the porosity is around 60%, the pore size is around 0.5mm, and the tissue grows typically in 5mm. Thus, we design the tensor field along the main compressive direction with the magnitudes gradually decrease from the shape boundary to the interior. (See Fig. 18.)

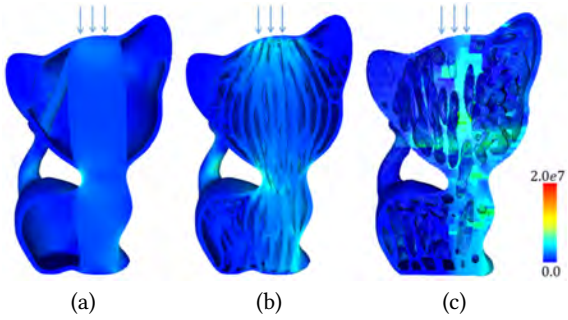

Figure 16: Comparison between the structures generated by topology optimization with a total volume constraint [Wu et al. 2016a] (a), and with local volume constraints [Wu et al. 2017] (b), and our method with the porosity constraints (c). The volume ratio is 45%, 44%, and 50% from left to right. Our yielding value in (c) is the same with (b), i.e., $\chi = 1.03e^7 N/m^2$.

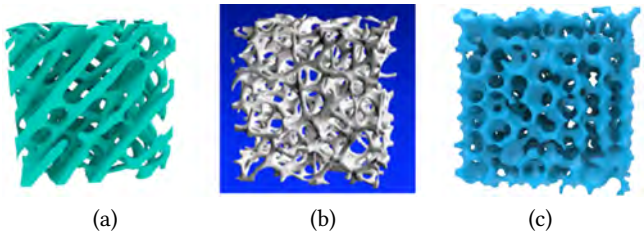

Figure 17: Visual comparison of a cubic sample from [Wu et al. 2017](a), a real bone sample from CT scans (Image courtesy of R. Müller [Müller and Rüegsegger 1997])(b), and our result (c).

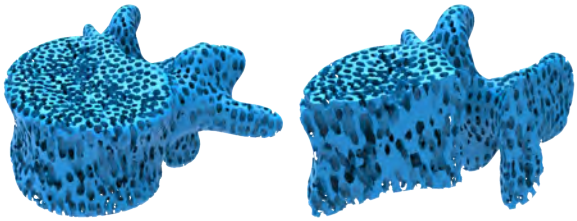

Figure 18: The porous vertebra model and its cross-section. The porosity is 60%.

6.6 Computational Cost and Fabrications

We tested our algorithm on a PC with a 4.01GHZ Core CPU, 16.0GB RAM, running Windows 10. The volumetric shape is discretized in voxels in the whole framework. In the implementations, the sampling rate is 100^3 within the bounding box.

The modeling framework and listed optimization are of computational efficiency except for the surface area optimization. During the strength optimization on (P, K), which is described in Section 6.4, only the combined function value is updated for each voxel and no need for the surface reconstruction. In the strength optimization process, FEM analysis is the most time-consuming part, which needs

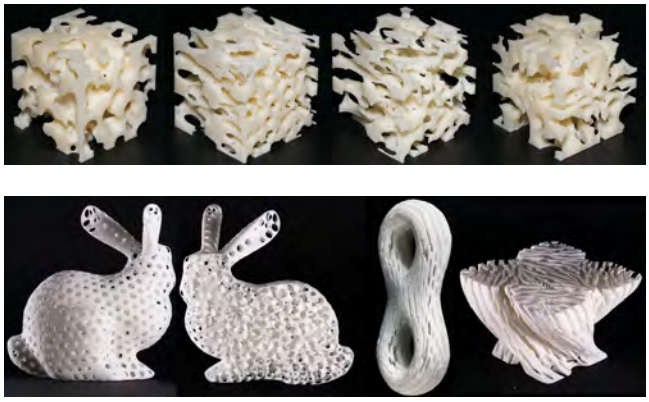

Figure 19: Some physical printouts. The first row is printed by an FDM printer. From left to right, the model from Fig. 10 ($\rho = 65\%$), Fig. 2 ($\rho = 60\%, 80\%$), and Fig. 7 ($\rho = 75\%$). The second row is printed by an SLS printer. The models are from Fig. 13.

3-5 minutes for 60K voxels. The number of iterations is influenced by the initial value of K and step size for decreasing each kernel size. It takes 20 to 30 iterations usually in our experiments.

Since the resulted porous structures are of both pore and solid connectivity, they can be fabricated by standard 3D printing techniques, such as FDM, SLS, SLM, and EBM, etc. Fig. 19 lists the 3D printed models using PLA-plastic material on an FDM printer or using nylon material on an SLS printer.

7 DISCUSSION, LIMITATIONS AND FUTURE WORK

Our paper provides a unified framework for modeling anisotropic, non-uniform, open-cell porous structures with organic pore shapes, considering both magnitude and directions of the given tensor field. The framework offers capabilities to control porous structures' properties by porosity, cell size, and cell shapes. We propose an MSC-based algorithm for ensuring the connections between both pores and solid components, via the guidance from the topology level, which we believe is the first of such attempt.

Gaussian kernels. Gaussian kernels naturally integrate the tensor matrix for each sample point, such that a global implicit function is defined in the volume. The level surface extracted from the global function is like the cellular structure. Such organic structures possess friendly properties like having sizeable internal surface areas, robustness for digital fabrication, etc.; however, they are not optimal concerning mechanical properties, compared with fine-grained topological optimization. It is worth to explore the potential for coordinating the oriented Gaussian kernels with the topology optimization framework, to achieve both tensor field awareness and optimal material occupancy.

MSC connections. MSCs naturally identify the local neighborhood for both pores and solid components through the ascending and descending manifolds. We remark that there might be alternatives to the fat curves for constructing the connections.

Material anisotropy. We mention that our anisotropy is on the structure level, not the material level. The material is homogeneous in our experiments. Our framework shares a similar philosophy of the inverse homogenization approach. Given a tensor field representing the physical properties, our method may generate the corresponding geometric structures. In many cases, to derive the relationship between target physical properties and tensor fields is itself a challenging problem.

Strength optimization. Optimization of the porous structures is a multiple-objective problem. Regarding the strength-to-weight criterion, our porous structure modeled based on the anisotropic Gaussian function is not the most efficient solution, as more materials are used to keep the cellular porosity comparing to topology optimization. Besides, voxel-based FE-analysis is not the best option in terms of accuracy and efficiency. We would like to investigate the multi-resolution finite element method in the future.

Future work. Aside from addressing limitations and possible extensions mentioned above, we expect to integrate the support-free constraints into our framework. We would like to adapt our framework to more applications, considering more physical properties or functionalities, like thermal conductivity, permeability, elasticity, etc. We also have an interest in investigating the relationships or mappings between physical properties and geometric structures.

ACKNOWLEDGMENTS

We thank all the anonymous reviewers for their valuable comments and constructive suggestions. This work is supported by grants from NSFC (61972232) and State Key Laboratory of Virtual Reality Technology and Systems (VRLAB2019A01).

REFERENCES

Rahul Arora, Alec Jacobson, Timothy R. Langlois, Yijiang Huang, Caitlin Mueller, Wojciech Matusik, Ariel Shamir, Karan Singh, and David I. W. Levin. 2019. Volumetric Michell trusses for parametric design & fabrication. In *Proceedings of the ACM Symposium on Computational Fabrication*. ACM. https://doi.org/10.1145/3328939.3328999

F. Cernuschi, I.O. Golosnoy, P. Bison, A. Moscatelli, R. Vassen, H.-P. Bossmann, and S. Capelli. 2013. Microstructural characterization of porous thermal barrier coatings by IR gas porosimetry and sintering forecasts. *Acta Materialia* 61, 1 (2013), 248 – 262. https://doi.org/10.1016/j.actamat.2012.09.055

Desai Chen, Mélina Skouras, Bo Zhu, and Wojciech Matusik. 2018. Computational discovery of extremal microstructure families. *Science Advances* 4, 1 (jan 2018), eaao7005. https://doi.org/10.1126/sciadv.aao7005

Lidija Čomić, Leila De Floriani, and Federico Iuricich. 2013. *Modeling Three-Dimensional Morse and Morse-Smale Complexes*. Springer Berlin Heidelberg, Berlin, Heidelberg, 3–34. https://doi.org/10.1007/978-3-642-34141-0_1

Leila De Floriani, Ulderico Fugacci, Federico Iuricich, and Paola Magillo. 2015. Morse complexes for shape segmentation and homological analysis: discrete models and algorithms. *Computer Graphics Forum* 34, 2 (2015), 761–785. https://doi.org/10.1111/cgf.12596

Qiang Du and Desheng Wang. 2005. Anisotropic Centroidal Voronoi Tessellations and Their Applications. *SIAM Journal on Scientific Computing* 26, 3 (2005), 737–761. https://doi.org/10.1137/S1064827503428527 arXiv:http://dx.doi.org/10.1137/S1064827503428527

J.H. Dunsmuir, S.R. Ferguson, K.L. D'Amico, and J.P. Stokes. 1991. X-Ray Microtomography: A New Tool for the Characterization of Porous Media. In *SPE Annual Technical Conference and Exhibition, 6-9 October, Dallas, Texas*. Society of Petroleum Engineers.

Herbert Edelsbrunner, John Harer, Vijay Natarajan, and Valerio Pascucci. 2003. Morse-smale Complexes for Piecewise Linear 3-manifolds. In *Proceedings of the Nineteenth Annual Symposium on Computational Geometry* (San Diego, California, USA) *(SCG '03)*. ACM, New York, NY, USA, 361–370. https://doi.org/10.1145/777792.777846

Lorna J. Gibson and M. F. Ashby. 1999. *Cellular solids : structure & properties* (2 edition ed.). Cambridge University Press. ix, 357 p. : pages.

A. Gyulassy and Vijay Natarajan. 2005. Topology-based simplification for feature extraction from 3D scalar fields. In *VIS 05. IEEE Visualization, 2005.* 535–542. https://doi.org/10.1109/VISUAL.2005.1532839

Attila Gyulassy, Vijay Natarajan, Valerio Pascucci, and Bernd Hamann. 2007. Efficient Computation of Morse-Smale Complexes for Three-dimensional Scalar Functions. *IEEE Transactions on Visualization and Computer Graphics* 13, 6 (Nov. 2007), 1440–1447. https://doi.org/10.1109/TVCG.2007.70552

R. Hilfer and C. Manwart. 2001. Permeability and conductivity for reconstruction models of porous media. *Physical Review E* 64 (Jul 2001), 021304. Issue 2. https://doi.org/10.1103/PhysRevE.64.021304

Y. Holdstein, A. Fischer, L. Podshivalov, and P. Z. Bar-Yoseph. 2009. Volumetric texture synthesis of bone micro-structure as a base for scaffold design. In *2009 IEEE International Conference on Shape Modeling and Applications*. 81–88. https://doi.org/10.1109/SMI.2009.5170167

Scott J. Hollister. 2005. Porous scaffold design for tissue engineering. *Nat Mater* 4, 7 (July 2005), 518–524. http://dx.doi.org/10.1038/nmat1421

X. Y. Kou and S. T. Tan. 2012. Microstructural Modelling of Functionally Graded Materials Using Stochastic Voronoi Diagram and B-Spline Representations. *Int. J. Comput. Integr. Manuf.* 25, 2 (Feb. 2012), 177–188. https://doi.org/10.1080/0951192X.2011.627948

MJ Kwiecien, IF Macdonald, and FAL Dullien. 1990. Three dimensional reconstruction of porous media from serial section data. *Journal of Microscopy* 159, 3 (1990), 343–359.

Hongwei Li, Li-Yi Wei, Pedro V. Sander, and Chi-Wing Fu. 2010. Anisotropic Blue Noise Sampling. *ACM Transactions on Graphics* 29, 6, Article 167 (Dec. 2010), 12 pages. https://doi.org/10.1145/1882261.1866189

Ruotian Ling, Jin Huang, Bert Jüttler, Feng Sun, Hujun Bao, and Wenping Wang. 2014. Spectral Quadrangulation with Feature Curve Alignment and Element Size Control. *ACM Transactions on Graphics* 34, 1, Article 11 (Dec. 2014), 11 pages. https://doi.org/10.1145/2653476

Xingchen Liu and Vadim Shapiro. 2015. Random heterogeneous materials via texture synthesis. *Computational Materials Science* 99 (2015), 177 – 189. https://doi.org/10.1016/j.commatsci.2014.12.017

Yang Liu, Wenping Wang, Bruno Lévy, Feng Sun, Dong-Ming Yan, Lin Lu, and Chenglei Yang. 2009. On Centroidal Voronoi Tessellation - Energy Smoothness and Fast Computation. *ACM Transactions on Graphics* 28, 4, Article 101 (Sept. 2009), 17 pages. https://doi.org/10.1145/1559755.1559758

Lin Lu, Andrei Sharf, Haisen Zhao, Yuan Wei, Qingnan Fan, Xuelin Chen, Yann Savoye, Changhe Tu, Daniel Cohen-Or, and Baoquan Chen. 2014. Build-to-last: Strength to Weight 3D Printed Objects. *ACM Transactions on Graphics* 33, 4, Article 97 (July 2014), 10 pages. https://doi.org/10.1145/2601097.2601168

C. Manwart and R. Hilfer. 1999. Reconstruction of random media using Monte Carlo methods. *Physical Review E* 59 (May 1999), 5596–5599. Issue 5. https://doi.org/10.1103/PhysRevE.59.5596

C. Manwart, S. Torquato, and R. Hilfer. 2000. Stochastic reconstruction of sandstones. *Physical Review E* 62 (Jul 2000), 893–899. Issue 1. https://doi.org/10.1103/PhysRevE.62.893

Jonàs Martínez, Jérémie Dumas, and Sylvain Lefebvre. 2016. Procedural Voronoi Foams for Additive Manufacturing. *ACM Transactions on Graphics* 35, 4, Article 44 (July 2016), 12 pages. https://doi.org/10.1145/2897824.2925922

Jonàs Martínez, Samuel Hornus, Haichuan Song, and Sylvain Lefebvre. 2018. Polyhedral Voronoi Diagrams for Additive Manufacturing. *ACM Transactions on Graphics* 37, 4, Article 129 (July 2018), 15 pages. https://doi.org/10.1145/3197517.3201343

Jonàs Martínez, Mélina Skouras, Christian Schumacher, Samuel Hornus, Sylvain Lefebvre, and Bernhard Thomaszewski. 2019. Star-shaped metrics for mechanical metamaterial design. *ACM Transactions on Graphics* 38, 4 (jul 2019), 1–13. https://doi.org/10.1145/3306346.3322989

Jonàs Martínez, Haichuan Song, Jérémie Dumas, and Sylvain Lefebvre. 2017. Orthotropic K-nearest Foams for Additive Manufacturing. *ACM Transactions on Graphics* 36, 4, Article 121 (July 2017), 12 pages. https://doi.org/10.1145/3072959.3073638

L.M. Mestetskii. 2000. Fat curves and representation of planar figures. *Computers & Graphics* 24, 1 (2000), 9 – 21. https://doi.org/10.1016/S0097-8493(99)00133-8

Lukas Mosser, Olivier Dubrule, and Martin J. Blunt. 2017. Reconstruction of three-dimensional porous media using generative adversarial neural networks. *Physical Review E* 96, 4 (oct 2017). https://doi.org/10.1103/physreve.96.043309

R. Müller and P. Rüegsegger. 1997. Micro-tomographic imaging for the nondestructive evaluation of trabecular bone architecture. *Studies in health technology and informatics* 40 (1997), 61–79.

Alisa Neeman, Boris Jeremic, and Alex Pang. 2005. Visualizing tensor fields in geomechanics. In *Visualization, 2005. VIS 05. IEEE*. IEEE, 35–42.

Jorge Nocedal and Stephen J Wright. 2006. *Numerical optimization. 2nd ed.* Springer.

Jonathan Palacios, Lawrence Roy, Prashant Kumar, Chen-Yuan Hsu, Weikai Chen, Chongyang Ma, Li-Yi Wei, and Eugene Zhang. 2017. Tensor Field Design in Volumes. *ACM Transactions on Graphics* (2017).

Julian Panetta, Qingnan Zhou, Luigi Malomo, Nico Pietroni, Paolo Cignoni, and Denis Zorin. 2015. Elastic Textures for Additive Fabrication. *ACM Transactions on Graphics* 34, 4, Article 135 (July 2015), 12 pages. https://doi.org/10.1145/2766937

L.M. Pant. 2016. *Stochastic Characterization and Reconstruction of Porous Media.* https://books.google.com/books?id=VcqGAQAACAAJ

J. Pouech, J. M. Mazin, and P. Tafforeau. 2010. High quality 3D imaging of vertebrate microremains using X-ray synchrotron phase contrast microtomography. *Comptes Rendus Palevol* 9, 6-7 (2010), 389–395.

Craig Schroeder, William C Regli, Ali Shokoufandeh, and Wei Sun. 2005. Computer-aided design of porous artifacts. *Computer-Aided Design* 37, 3 (2005), 339–353.

Christian Schumacher, Bernd Bickel, Jan Rys, Steve Marschner, Chiara Daraio, and Markus Gross. 2015. Microstructures to Control Elasticity in 3D Printing. *ACM Transactions on Graphics* 34, 4, Article 136 (July 2015), 13 pages. https://doi.org/10.1145/2766926

Nithin Shivashankar and Vijay Natarajan. 2012. Parallel Computation of 3D Morse-Smale Complexes. *Computer Graphics Forum* 31, 3pt1 (2012), 965–974. https://doi.org/10.1111/j.1467-8659.2012.03089.x

Ole Sigmund. 1994. Materials with prescribed constitutive parameters: An inverse homogenization problem. *International Journal of Solids and Structures* 31, 17 (1994), 2313 – 2329. https://doi.org/10.1016/0020-7683(94)90154-6

Wei Sun, Binil Starly, Jae Nam, and Andrew Darling. 2005. Bio-CAD modeling and its applications in computer-aided tissue engineering. *Computer-Aided Design* 37, 11 (2005), 1097–1114.

Davi C. Tozoni, Zhongshi Jiang, Julian Panetta, and Daniele Panozzo. 2020. A Low-Parametric Rhombic Microstructure Family for Irregular Lattices. In *ACM SIGGRAPH 2020*.

Weiming Wang, Tuanfeng Y. Wang, Zhouwang Yang, Ligang Liu, Xin Tong, Weihua Tong, Jiansong Deng, Falai Chen, and Xiuping Liu. 2013. Cost-effective Printing of 3D Objects with Skin-frame Structures. *ACM Transactions on Graphics* 32, 6, Article 177 (Nov. 2013), 10 pages. https://doi.org/10.1145/2508363.2508382

W J Whitehouse and E D Dyson. 1974. Scanning electron microscope studies of trabecular bone in the proximal end of the human femur. *Journal of Anatomy* 118, Pt 3 (Dec. 1974), 417–444. http://www.ncbi.nlm.nih.gov/pmc/articles/PMC1231543/

Chengtie Wu, Yongxiang Luo, Gianaurelio Cuniberti, Yin Xiao, and Michael Gelinsky. 2011. Three-dimensional printing of hierarchical and tough mesoporous bioactive glass scaffolds with a controllable pore architecture, excellent mechanical strength and mineralization ability. *Acta Biomaterialia* 7, 6 (2011), 2644 – 2650. https://doi.org/10.1016/j.actbio.2011.03.009

J. Wu, N. Aage, R. Westermann, and O. Sigmund. 2017. Infill Optimization for Additive Manufacturing – Approaching Bone-like Porous Structures. *IEEE Transactions on Visualization and Computer Graphics* PP, 99 (2017), 1–1. https://doi.org/10.1109/TVCG.2017.2655523

J. Wu, C. Dick, and R. Westermann. 2016a. A System for High-Resolution Topology Optimization. *IEEE Transactions on Visualization and Computer Graphics* 22, 3 (March 2016), 1195–1208. https://doi.org/10.1109/TVCG.2015.2502588

Jun Wu, Charlie C.L. Wang, Xiaoting Zhang, and Rüdiger Westermann. 2016b. Self-supporting rhombic infill structures for additive manufacturing. *Computer-Aided Design* 80, Supplement C (2016), 32 – 42. https://doi.org/10.1016/j.cad.2016.07.006

Jun Wu, Weiming Wang, and Xifeng Gao. 2019. Design and Optimization of Conforming Lattice Structures. (2019). https://doi.org/10.1109/TVCG.2019.2938946 arXiv:1905.02902v1 [cs.CE]

Brian Wyvill, Paul G Kry, Raimund Seidel, and David Mould. 2012. Determining an aesthetic inscribed curve. In *Proceedings of the Eighth Annual Symposium on Computational Aesthetics in Graphics, Visualization, and Imaging*. Eurographics Association, 63–70.

Ulas Yaman, Nabeel Butt, Elisha Sacks, and Christoph Hoffmann. 2016. Slice Coherence in a Query-based Architecture for 3D Heterogeneous Printing. *Comput. Aided Des.* 75, C (June 2016), 27–38. https://doi.org/10.1016/j.cad.2016.02.005

X. Yan, C. Rao, L. Lu, A. Sharf, H. Zhao, and B. Chen. 2019. Strong 3D Printing by TPMS Injection. *IEEE Transactions on Visualization and Computer Graphics* (2019), 1–1. https://doi.org/10.1109/TVCG.2019.2914044

Jianming Ying, Lin Lu, Lihao Tian, Xin Yan, and Baoquan Chen. 2018. Anisotropic porous structure modeling for 3D printed objects. *Computers & Graphics* 70 (2018), 157 – 164. https://doi.org/10.1016/j.cag.2017.07.008 CAD/Graphics 2017.

Dongjin Yoo. 2011. Porous scaffold design using the distance field and triply periodic minimal surface models. *Biomaterials* 32, 31 (2011), 7741 – 7754. https://doi.org/10.1016/j.biomaterials.2011.07.019

Eugene Zhang, James Hays, and Greg Turk. 2007. Interactive tensor field design and visualization on surfaces. *Visualization and Computer Graphics, IEEE Transactions on* 13, 1 (2007), 94–107.

Hui Zhang, Weikai Chen, Bin Wang, and Wenping Wang. 2017. By Example Synthesis of Three-dimensional Porous Materials. *Comput. Aided Geom. Des.* 52, C (March 2017), 285–296. https://doi.org/10.1016/j.cagd.2017.03.015

Zichun Zhong, Xiaohu Guo, Wenping Wang, Bruno Lévy, Feng Sun, Yang Liu, and Weihua Mao. 2013. Particle-based Anisotropic Surface Meshing. *ACM Transactions on Graphics* 32, 4, Article 99 (July 2013), 14 pages. https://doi.org/10.1145/2461912.2461946

Xiaolei Zhu, Shigang Ai, Xiaofeng Lu, Ke Cheng, Xiang Ling, Lingxue Zhu, and Bin Liu. 2014. Collapse models of aluminum foam sandwiches under static three-point bending based on 3D geometrical reconstruction. *Computational Materials Science* 85, 0 (2014), 38–45.